LUND UNIVERSITY
Faculty of Science

Electron Assisted Growth of Graphene atop Ir(111) supported Hexagonal Boron Nitride

Lassi Linnala

Thesis submitted for the degree of Bachelor of Science
Project duration: 3 months

Supervised by Jan Knudsen

Department of Physics
Division of Synchrotron Radiation Research
January 2019

Abstract

Vertical heterostructures between graphene (Gr) and hexagonal boron nitride (hBN) have attracted a great deal of interest, due to their potential applications in the semiconductor industry as new and superior transistor materials. The direct growth of the heterostucture still remains challenging and in this bachelor thesis, I report a novel electron assisted growth technique, which is used to attempt to grow Gr atop hBN atop an Ir(111) single crystal surface. This technique has already proven to be successful in the opposite order of growing hBN atop Gr/Ir(111) [1].

To properly understand the growth and possible heterostructure formation, pure phases of both hBN and Gr on Ir(111) are characterized first using scanning tunneling microscopy (STM) and low energy electron diffraction (LEED). This structural characterization of the pure phases reveals a stronger binding of hBN than Gr to Ir(111) and, therefore, a favored stacking order of Gr atop hBN.

In contrast to this expectation, my STM and LEED results of the electron assisted growth of Gr atop a full hBN layer show, that the temperature required for Gr formation is too high for hBN layer to sustain, and is already complicated by a low sticking coefficient of ethylene atop. After high temperature annealing, the hBN layer is determined to leave behind a (6×2) boron nanoribbon superstructure and no ordered Gr islands are observed. However, the effect of the electron beam in the growth technique is indicated to result in an uneven charging of the hBN layer on Ir(111), and this, in combination with its already highly corrugated pore-wire structure, calls for new research.

Acknowledgements

First and foremost, I want to thank my supervisor Jan Knudsen. Thank you for teaching me everything I know about surface science and already evoking my interest to the exciting field of two-dimensional materials during the surface science course. Thank you further, for offering me an opportunity to be part of a real research project and for all the discussions we had, always providing me with clear answers to all my questions.

I want to also thank Virginia for teaching me everything I know about working in an STM lab and sharing the, sometimes long, lab hours with me. Thank you also, for all the valuable advice on how to plan and complete this project, always providing me positive influence and advice at some occasional times of hardships.

Contents

Abbreviations

2DMs - Two-Dimensional Materials
Gr - Graphene
hBN - Hexagonal Boron Nitride
STM - Scanning Tunneling Microscopy
LEED - Low Energy Electron Diffraction
CVD - Chemical Vapor Deposition
EAG - Electron Assisted Growth
TPG - Temperature Programmed Growth
vdW - van der Waals
UHV - Ultra-High Vacuum
S.E - Schrödinger Equation
TH - Tersoff-Hamann
LDOS - Local Density of States
DFT - Density Functional Theory
RT - Room Temperature
FFT - Fast Fourier Transform
XPS - X-Ray Photoelectron Spectroscopy

1 Introduction

Two-dimensional materials (2DMs), such as graphene (Gr), have attracted a great deal of attention due to their unique properties. Properties, that are inaccessible in their three-dimensional counterparts and which could lead to a variety of possible applications. As a result of extensive research, a lot has been achieved since Gr was first isolated from the van der Waals (vdW) bound bulk graphite in 2004 by mechanical exfoliation [2]. In comparison to Gr, hexagonal boron nitride (hBN) is rather unknown. In the same year, or rather, almost a year earlier, Corso et al. [3] reported a discovery of so-called boron nitride nanomesh on Rh(111) grown by chemical vapor deposition (CVD), that is, by dosing a precursor molecule borazine onto a hot, clean and catalytically active Rh(111) substrate. However, as the field of 2DMs still was to be arisen by the discovery of Gr, this hBN/Rh(111) nanomesh structure was first explained as a few atomic layers of hBN. Only a few years later it was suggested [4] and verified [5] to consist only of single atomic layer of hBN.

Majority of the low-hanging fruits have already been picked in terms of the growth, structure and properties of individual 2DMs. Therefore, a large research effort has been shifted to investigate how the individual 2DMs could be stacked together to form, so-called vertical vdW heterostructures. The two isostructural and isoelectronic, sp^2 hybridized honeycomb structures hBN and Gr are, for example, interesting to stack. Graphene itself is well known for its extremely high carrier mobility, due to the linearly dispersing Dirac cone band structure, and hence massless Dirac fermions [6]. Unfortunately the zero band gap, making it impossible for Gr to stand by itself within the electronic industry. However, combined with hBN, where the interplay of alternating B and N atoms creates a bandgap of 5.97 eV, the highly desired semiconducting properties could be achieved. Therefore, Gr/hBN heterostructures have promising applications varying from electronics to photonics [7, 8]. In particular, it has already been shown that using few layers of hBN as the dielectric material in a graphene field-effect-transistor does not diminish its properties [9], as opposed to some other dielectric substrates, and in some cases, hBN can even further enhance them [10].

Figure 1(a) can be conceptually used to vizualize the vertically stacked vdW heterostructure between the two honeycomb structures. Intrinsically, the figure shows the hBN bulk structure, where the strongly covalent bound atomic layers are bound together by weak vdW bonds. Now, by replacing the B and N atoms in one layer by carbon atoms, one has the Gr/hBN vdW heterostructure, and by further continuing one reaches the graphite structure. Even though the vast similarities in their structures, they do differ by a mismatch of approximately 1.8 % in their surface lattice constants. If the two atomic layers are aligned on top of each other, this lattice mismatch will give arise to a characteristic "beating pattern", visualized in Fig 1(b).

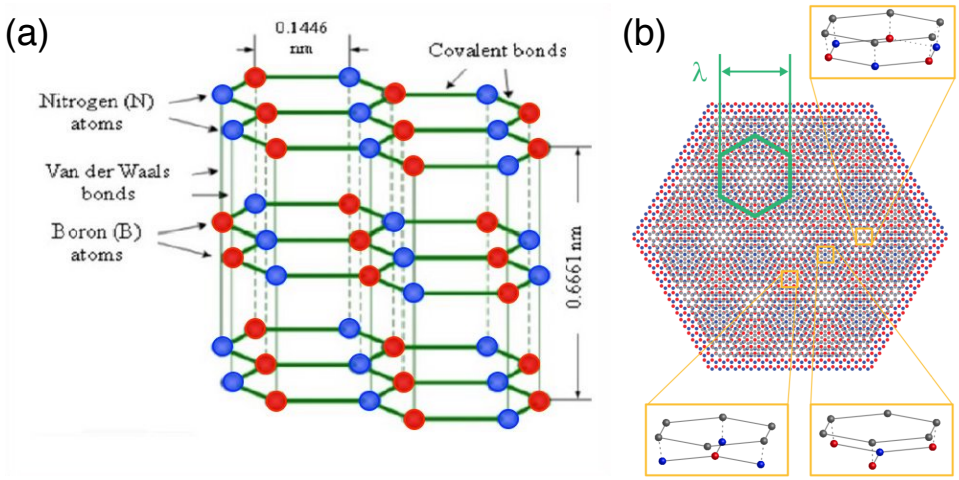

Figure 1: (a) Van der Waals bound bulk hBN [11]. (b) Schematic moiré superstructure of the Gr/hBN heterostructure [12].

This periodic beating pattern, better known as a moiré superstructure, already present in any epitaxial 2DMs, and its periodic distance is denoted by the moiré lattice constant λ. In the Fig. 1(b) are also marked high-symmetry sites, where the atoms of the two layers are stacked in a specific stacking order. The repetition of these sites in the heterostructure will result in periodic variations in the superlattice potential, and can ultimately even lead to fundamentally new physics, such as fractional quantum Hall effect and theorized Hofstadter butterfly effect [12].

Even though, epitaxial growth of high quality monolayers of both Gr and hBN on transition metal substrates are a rather common practice today, the direct growth of the second layer remains challenging. This is simply because of the fact, that by covering the catalytically active substrate with the first monolayer of inert sp^2 hybridized layer, either Gr or hBN, no second layer can be grown by the commonly used CVD technique or its direct derivatives. In these techniques, the catalytic activity of the substrate is of crucial importance to dissociate the precursor molecules. Therefore, improved growth techniques are fundamental for manufacturing these heterostructures. Even the already discussed, realized applications of Gr/hBN vdW heterostructures, consists of thin films of either Gr, hBN or both, commonly manufactured by direct transfer i.e., mechanical exfoliation [13]. This technique, however, gives no control of the amount of stacked layers, and is not promising to be implemented beyond the field of research. Furthermore, the electronic structure of bilayer Gr is already vastly different to monolayer Gr [6].

In this thesis, full advantage of the catalytic activity of Ir(111) substrate is used for growing the first monolayer of hBN. The Ir(111) substrate further provides a well defined reference for the structural characterization of hBN by scanning tunneling microscopy (STM) and low energy electron diffraction (LEED). In particular, the characteristic moiré structure of the epitaxial hBN, already present as a result of the lattice mismatch between hBN/Ir(111) will be determined and discussed. The influence of the substrate and the periodic variations in the lateral atomic registry will also be discussed, and compared to the structure of Gr on Ir(111). Finally, it will be attempted to grow the vertical vdW heterostructure of Gr atop hBN/Ir(111), employing a novel technique, namely, electron

assisted growth (EAG). In this technique an electron beam will assist to dissociate the hydrocarbons from the common Gr precursor ethylene already at room temperature (RT). The growth will be initiated by a step-wise annealing and STM and LEED characterization of the possible Gr formation will be discussed.

2 Theory

In this section an important concept of crystal structures are described, followed by both a theoretical and an experimental description of surface techniques that are used to probe these structures in this thesis.

2.1 Real and Reciprocal Space

In a real three-dimensional vector space, a real Bravais lattice is defined as a discrete set of points with position vectors of the form,

$$\mathbf{R} = n_1\mathbf{a_1} + n_2\mathbf{a_2} + n_3\mathbf{a_3} \tag{1}$$

where $\{\mathbf{a}_i\}$ are linearly independent, primitive translation vectors that span the Bravais lattice for $n_i \in \mathbb{Z}$. The Bravais lattice combined with basis atoms gives the crystal structure. Translational symmetry of the Bravais lattice allows for a mathematical construction of a dual-space, namely, a reciprocal space.

The reciprocal space can be defined as a Fourier transform (FT) of the real space, i.e., any real Bravais lattice periodic function can be expanded as Fourier series to reciprocal space. Take, for example, an arbitrary function in a 1D lattice with spacing a,

$$f(x) = f(x+a) \overset{FT}{\Longrightarrow} \sum_k f_k e^{ikx} = \sum_k f_k e^{ikx} e^{ika} \tag{2}$$

where $k = n2\pi/L$ for $n \in \mathbb{Z}$ with $L \equiv [\mathrm{m}]$, and f_k are the Fourier coefficients. For the last equality to hold, it has to be satisfied that $\exp(ika) = 1$, which gives $k = n2\pi/a$. In general, considering a 3D Bravais lattice periodic function $f(\mathbf{r}) = f(\mathbf{r} + \mathbf{R})$, and one has

$$e^{i\mathbf{G}\cdot\mathbf{R}} = 1 \tag{3}$$

where $\mathbf{G} = h\mathbf{a_1^*} + k\mathbf{a_2^*} + l\mathbf{a_3^*}$ for $h, k, l \in \mathbb{Z}$, is by definition the corresponding Bravais lattice in reciprocal space. For the above identity to hold it can be shown, that the real and reciprocal lattice vectors must satisfy,

$$\mathbf{a_i^*} \cdot \mathbf{a_j} = 2\pi\delta_{ij} \tag{4}$$

where δ_{ij} is the Kronecker's delta. This equation now constructs the whole reciprocal lattice from the real lattice and vice versa. However, even the orthogonality of the lattice vectors and therefore, possible rotations between the two lattices are not completely necessary for the present thesis. It is often enough to note the "reciprocity", namely,

$$|\mathbf{a}_i^*| \propto \frac{1}{|\mathbf{a}_i|} \tag{5}$$

as already evident from the 1D case.

2.2 Surface Techniques

To carry out surface science experiments it is not only necessary to have special techniques with high enough surface sensitivity, but it is also crucial to be able to keep the surface under investigation clean for a long enough time. The latter condition and also indirectly the former, can be achieved by operating in an ultra-high vacuum (UHV) environment. The UHV environment typically has a pressure in the order of 10^{-10} mbar or below, which can maintain the surface relatively clean for several hours. This low pressure can be achieved by using several pumping techniques in series, namely, rough, turbo and ion pumps. For more details see e.g.[14].

The two surface techniques described in this section are LEED and STM. They are both electron based techniques and, therefore, surface sensitive. However, it is important to note that STM is a local probe while LEED is an averaging scattering technique.

2.2.1 Low Energy Electron Diffraction

Electrons are known to have a wavelength given by the de Broglie equation

$$\lambda = \frac{h}{\sqrt{2mE}} \tag{6}$$

where h is Planck constant, m is the electron rest mass and E is the electron kinetic energy. For typical energy range used in LEED; 20-200 eV, this gives a wavelength in the order of ångströms, just small enough to probe atomic distances in crystal structures. Furthermore, due to the wave nature of electrons, the propagation of an incident electron in LEED can be described by a wavevector

$$\mathbf{k}_0 = \frac{\sqrt{2meU}}{\hbar}\hat{\mathbf{k}} \tag{7}$$

where $\hbar$ is reduced Planck constant, U is the accelerating voltage and e is the electron charge. Based on von Laue conditions for elastic scattering, $|\mathbf{k}_0| = |\mathbf{k}|$, it is known that constructive interference as a result of scattering from real lattice vector occurs, if and only if the change in wavevector is equal to the reciprocal lattice vector,

$$\Delta\mathbf{k} = \mathbf{k}_0 - \mathbf{k} = \mathbf{G}_{hkl} \tag{8}$$

where $\mathbf{k}$ is the scattered wavevector. From this, Eq. (8), it is noted that the diffraction pattern satisfies all the reciprocal lattice relations described in the previous section.

In Fig. 2(a) is shown schematics of a typical LEED setup. A monochromatic low kinetic energy electron beam is generated by a filament and accelerated by voltage U towards a sample. The electron beam is further focused by electron optics, achieving a beam diameter of approximately 1 mm. The low kinetic energy electrons heavily interact with the sample and are then backscattered either elastically or inelastically. On the way back towards the detector, the electrons encounter multiple grids all of which are grounded

to provide field free regions, except the one indicated by number 2. This grid is biased with a voltage just above the initial accelerating voltage and, therefore, only lets through elastically scattered electrons. Finally, the electrons are detected on a fluorescent screen. The fluorescent screen is biased with a high voltage to again accelerate the electrons which then gives an intense light pulse for each electron. The screen is further curved, or rather spherical, to provide an uniform scattering radius from the sample.

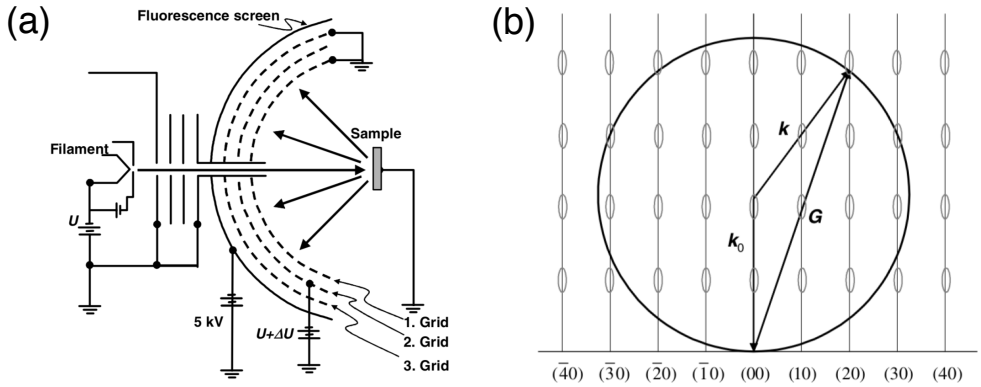

Figure 2: (a) Schematics of a typical LEED setup (b) Ewald sphere construction fulfilling the Laue conditions for elastic scattering in two dimensions. Indicated are vertical crystal truncation rods indexed by the Miller indices (h,k). The fluorescent screen corresponds to the top part of the sphere normal to electron incidence $\mathbf{k}_0$. Both from [15]

Figure 2(b) shows an Ewald sphere construction of the Laue conditions in the reciprocal lattice hl-plane. The fluorescent screen is the top part of the circle, normal to the wavevector of the incident electrons $\mathbf{k}_0$. The sphere radius can be varied by varying the accelerating voltage given by Eq. (7), and the Laue conditions are met when the circle intersects the vertical rods. These vertical rods are due to symmetry breaking at the surface, because of which the three Laue conditions are reduced to two, i.e., Eq. (8) becomes $\Delta\mathbf{k} = \mathbf{G}_{hk}$, and diffraction spots are observed for the whole range of kinetic energies. However, the inelastic free mean path for low kinetic energy electrons, 20-200 eV, is in the order of 5-10 Å, i.e., few atomic layers. Therefore, rather sharp intensity maximas are observed when the circle intersects the denoted ellipsoids, corresponding to the bulk Laue conditions. It is to be noted, that these conditions do not explain intensity fluctuations observed in experimental LEED patterns as a function of the electron kinetic energy.

In the simplest case, LEED can serve as a quick macroscopic technique to determine symmetries and periodicities of possible overlayer structures in the system, as used throughout in this thesis. However, not always explicitly as shown in an example below. The most common way to describe overlayer structures is Wood's notation,

$$\left(\frac{|\mathbf{b}_1|}{|\mathbf{a}_1|} \times \frac{|\mathbf{b}_2|}{|\mathbf{a}_2|}\right) \mathrm{R}\alpha - \mathrm{A} \tag{9}$$

where $\mathbf{a}_i$ are the substrate unit cell vectors and $\mathbf{b}_i$ are the overlayer vectors, α denotes possible rotation between these vectors and A corresponds to a chemical element.

Figure 3(a) shows real space overlayer structures of (2×2)R0 and three rotational domains of (2×1)R0 on fcc(111). Noting that the ratios of the lengths in the Wood notation can be simply inverted to correspond to reciprocal space. This real space structure can then be characterized in a typical LEED image shown in Fig. 3(b), where the unit cell vectors of the fcc(111) are indicated by the white arrows. The three different colors corresponding to the different rotational domains of the (2×1)R0 structures. However, without the color coding it would be impossible to distinguish whether the LEED pattern is actually from a (2×2) structure or the three rotational domains of (2×1) structures.

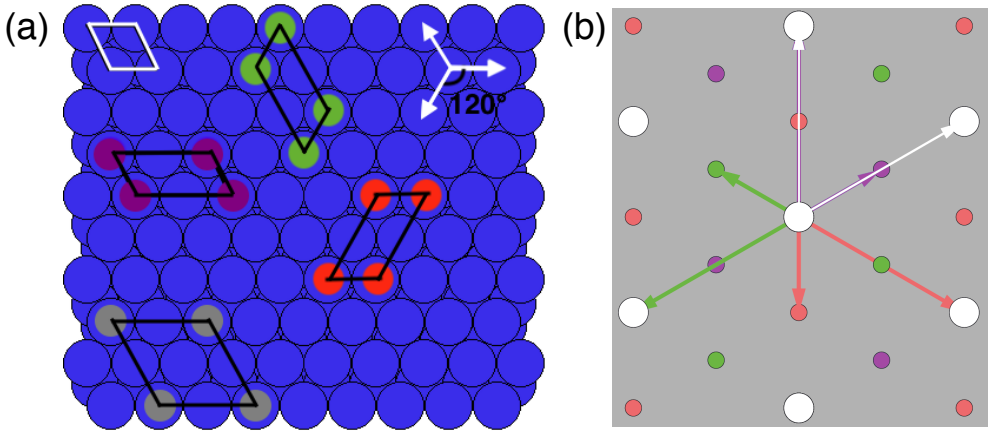

Figure 3: Real and reciprocal space structural characterizations (a) Hexagonal substrate, (2×2) and three rotational domains of (2×1) overlayer structures (b) Schematic LEED pattern corresponding to three coexisting rotational domains of (2×1) overlayer structures, from [16].

Further complications to the structural determination with LEED is caused by intensity variations of the diffraction spots as a function of the electron kinetic energy. Sometimes making some spots hardly visible, if at all, especially in the case of low coverage. It is always important to record images for a range of different kinetic energies. Moreover, sometimes even multiple scattering events have to be considered, especially in the case of layered structures or with possible sub-structures inside the unit cell.

Additionally, one can note by comparing these two figures for real and reciprocal lattices of fcc(111) that there is 30° rotation between them. This is caused by the orthogonality of the real and reciprocal lattice vectors of different indices as described by the Eq. (4), which can be further used to distinguish the different domains.

2.2.2 Scanning Tunneling Microscopy

Scanning tunneling microscope is one of the common real space surface techniques in the family of scanning probe microscopes. The technique is fairly new surface technique compared to scattering techniques and was invented by Binning and Rohrer in 1983 [17]. As the name suggests, this technique and its surface sensitivity combined with "atomic" resolution relies all on quantum tunneling. That is, an electron can tunnel through a classically forbidden region, i.e., through a potential barrier between an atomically sharp STM tip and the surface being probed. As the operation principle is based on quantum mechanics, it can be described by the many-body Schrödinger equation (S.E),

$$\hat{H}\Psi = E\Psi \tag{10}$$

where the Hamiltonian operator, $\hat{H} = \hat{T} + \hat{U}$, is the sum of kinetic and potential energy operators. If one could solve for the energy eigenvalues E, and the corresponding eigenstates Ψ, any observable quantity of the system could be determined, in principle.

To conceptually understand the operation principle of STM, it is, however, enough to restrict to tunneling in 1D, in the simplest approximation as follows. Considering a free electron travelling to +z-direction, and which encounters a finite constant potential $U(z) = U$ for $0 \leq z < d$, further assuming no reflection. The electronic wavefunction $\psi(z)$ solving a single electron S.E is given by $\psi(z) = \psi(0)\exp(-\kappa z)$, where the decay constant is $\kappa = \sqrt{2m(U-E)}/\hbar$. Furthermore, the transmission through this barrier of width d is given by $T = \exp(-2\kappa d)$.

In STM operation, the apparent potential barrier height can be approximated as the average of the tip and sample work functions, i.e., $U = \Phi_b = (\Phi_t + \Phi_s)/2$ [18]. For simplicity, assuming equal conductors and estimating typical metal work functions, $\Phi_b = 4$ eV $\gg E$, gives a decay constant of $\kappa = \sqrt{2m\Phi_b}/\hbar = 1$ Å^{-1}. Therefore, for every $\Delta d = 1$ Å this results in a decay of the tunneling current by almost an order of magnitude. It is now clear why technique based on quantum tunneling is so powerful. For flat surfaces, approximately 90 % tunneling can be accounted coming from the outermost tip atom only, (of the atomically sharp tip), giving this technique an extremely high resolution.

However, to further understand what is actually imaged in the STM, one has to turn back to the many-body S.E. Commonly adopted approach to discuss the theory behind STM is Tersoff-Hamann theory [19], which is based on the many-body tunneling theory of Bardeen [20]. Neglecting electron-electron interaction, Bardeen solved the S.E for the "tip" and the sample separately as one particle equations. Assuming weak tip-sample interaction and nearly orthogonal states and, therefore, by time-dependent perturbation theory, the tunneling current to the first order can be written as,

$$I = \frac{2\pi e}{\hbar}\sum_{t,s} f(E_t)[1 - f(E_s + eV)]|M_{ts}|^2\delta(E_t - E_s) \tag{11}$$

where, in terms of Fermi-Dirac distribution, $f(E_t)[1-f(E_s+eV)]$ is the probability of an occupied and an empty state existing at the tip, E_t, and sample, E_s, energies, combined with an applied bias V. The Dirac delta function $\delta(E_t - E_s)$ allows only elastic transitions. M_{ts} is the matrix element describing the overlap of the tip and sample states subjected to the perturbation. This equation is simply the Fermi's golden rule; a general result of the time-dependent perturbation theory, describing the transition rate from one eigenstate to another, further fulfilling the tunneling condition from filled states to empty states.

Using Bardeen's transfer Hamiltonian method, the matrix element can be written as a current density operator, integrated over any surface area in the barrier region bounding the volume between tip and sample,

$$M_{ts} = \frac{\hbar^2}{2m}\int d\mathbf{S}(\psi_t^*\nabla\psi_s - \psi_s\nabla\psi_t^*) \tag{12}$$

The matrix element and hence, the tunneling current can be solved separately from the tip and the sample S.Es. No knowledge of the total Hamiltonian or the total wavefunctions

is required. For two well defined surfaces, both wavefunctions can be expanded as Bloch surface states, however, in STM operation the exact structure of the atomically sharp tip is not known. Therefore, the tip states are hard to determine.

After the invention of STM, Tersoff-Hamann (TH) made further approximations to this theory, namely, low operation bias; decreasing the tunneling energy interval, low temperature limit; all states are occupied(unoccupied) below(above) the Fermi level and most importantly approximating spherical, s-wave tip. This s-wave tip approximation naturally made the evaluation of the Eq. (12) almost trivial. Under these approximations, the tunneling current can be written as,

$$I \propto V \sum_{s} |\psi_s(\mathbf{r}_0)|^2 \delta(E_s - E_f) = V \rho_s(\mathbf{r}_0, E_f) \tag{13}$$

The tunneling current is now proportional to the applied bias V and the local density of states (LDOS), $\rho(\mathbf{r}_0, E_f)$, of the sample at the Fermi level E_F, evaluated at the position of the tip. Therefore, in the TH picture the STM does not image the surface atoms, but rather the electronic structure convoluted with the tip height. It is also to be mentioned, that this theory makes the simulation of STM images rather trivial as the only unknown is the LDOS of the sample at a certain height, which is trivially determined within any electronic structure simulation, such as density functional theory (DFT). Furthermore, this theory allows interpretation of STM images way beyond just the structure.

However, there are several shortcomings to this theory, namely: It is not possible to describe often experimentally observed strong tip-sample interaction, especially in the case of low tip-sample distances, or constantly varying tunneling conditions, where the former already inherent from Bardeen's perturbation theory approach. Moreover, even the minimum lateral resolution given by Tersoff-Hamann's s-wave tip approximation cannot explain the often experimentally achieved atomic resolution. The tip states have been further modified to the Bardeen theory by Chen [21], where it was determined, that the atomic resolution cannot only be accounted for the atomic sharpness of the tip, but rather for using a tip material with partially filled d-shell, such as tungsten. For which the atomic resolution was determined to occur when the tunneling is from tungstens d_{z^2} orbitals [22].

Figure 4(a) shows schematics of the tunneling principle from filled states to empty states between two conductors, separated by a distance d. The red wave shows the overlap of the real part of two Bloch waves through a potential barrier of height, given as the average of the two work functions. Furthermore, as a negative bias is applied to one conductor, it will raise its Fermi level, E_F, respect to the other conductor, giving electrons enough energy to tunnel from the filled states of one conductor to the empty states of the other. If the direction of the bias is reversed, the tunneling principle is reversed, i.e., the STM can be used to probe both the filled and the empty states of the sample.

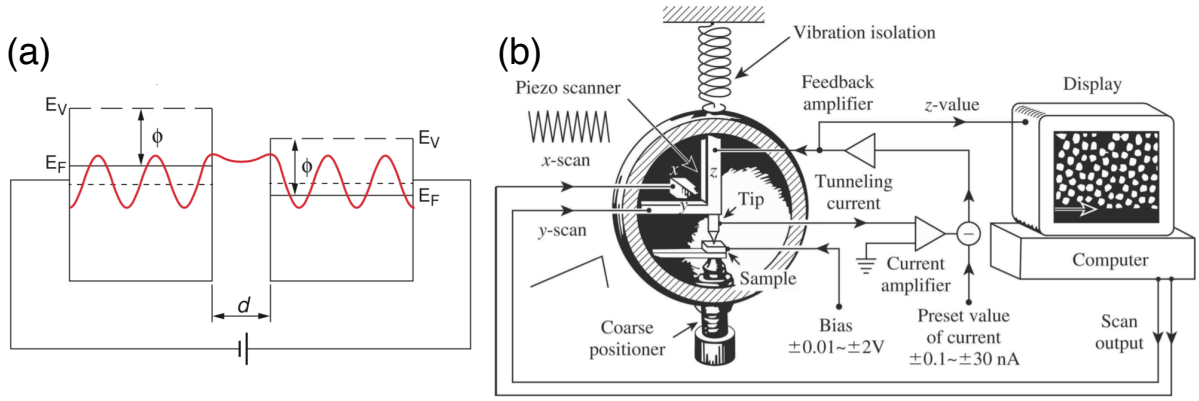

Figure 4: (a) Tunneling between two biased conducting materials separated by a distance d [14]. (b) Schematics of a typical STM setup [23].

Figure 4(b) shows schematics of a typical STM setup. Atomically sharp tip is connected to a xyz-piezoelectric tripod and is approached within a nanometer distance from the sample surface in UHV chamber. A raster scan, performed by the x and y pods, is initiated from the computer while a small bias is applied to the sample. If the bias applied to the sample is negative, the electrons will tunnel from the sample to the tip and a tunneling current is measured at every point of the scan. Two scanning modes exist, namely, constant current mode and constant height mode. In the constant current mode, used in this thesis, a preset current value is chosen and the measured tunneling current is compared to this value at every point of the scan. To maintain the chosen constant current value, a correction voltage is applied to the z-piezo, either expanding or contracting it, and the tunneling current will increase or decrease exponentially as a result. This applied correction voltage can be directly converted to a topographic image of the surface, which is then viewed on the computer. With correct calibration on known substrates, the piezos response to the correction voltage can be converted to a surface topographic image with a very high resolution.

In a constant-height mode, the feedback loop is kept idle and the tunneling current variation is measured instead. This method is generally faster, but often results in tip crashes due to high topographical variations of surfaces. Furthermore, the STM has to be isolated from vibrations coming from the surroundings, which can be achieved by either floating the sample in a magnetic field or by spring damping as illustrated in the figure.

3 Method

All experiments were carried out in the Obelix UHV environment with base pressure of 10^{-10} mbar at Lund University. This environment consisted of a preparation chamber and an analysis chamber, where the latter is equipped with room temperature STM and LEED. The Ir(111) single crystal was cleaned by repeated cycles of annealing at 1400 K, hot sputtering with 1 kV Ar^+ ions at 1000 K ($p = 10^{-5}$ mbar, $HV = 650$ V, $I_{ems} = 10$ mA) and exposing to system to oxygen atmosphere of pressure $p = 10^{-7}$ mbar at 800 K.

Growth hBN/Ir(111): Prior to the hBN growth, the precursor borazine was purified by three cycles of freeze-pumb-thaw. The hBN monolayer was grown by CVD, exposing the Ir(111) substrate to 100 L of borazine ($p = 10^{-6}$ Torr for 100 s) at 1250 K in the preparation chamber. The high quality of the grown hBN monolayer was verified with STM and LEED and is discussed in Sec. 4.2.

Growth Gr/hBN/Ir(111): The electron beam from the filament, (I = 4 A and HV = 200 V), in the EAG technique was used to dissociate the hydrocarbons from the precursor molecule ethylene. Two doses, followed by step-wise annealing were characterized, namely: Dose 300 L ethylene ($p = 10^{-6}$ Torr for 300 s at RT), anneal in steps of 773 K, 1073 K and 1273 K. Start over by cleaning the sample and growing hBN with the above recipe, then: Dose 6000 L ethylene ($p = 10^{-5}$ Torr for 600 s at RT), anneal in steps of 773 K, 973 K, 1173 K and 1373 K. STM and LEED characterization were performed after every step. The temperatures were carefully measured using infrared pyrometer. This temperature evolution is discussed in Sec. 4.3. Furthermore, the acquired STM and LEED images were processed and analyzed using ImageJ and Igor Pro softwares.

4 Results and Discussion

4.1 Substrate Ir(111)

The substrate chosen for the growth of the Gr/hBN heterostructure was Ir(111). Iridium is a group 9 element, just below rhodium in the periodic table of elements, hence with a partially filled d-shell a transition metal by definition. Iridium has a high melting point of 2700 K which makes the high temperature growth of Gr/hBN possible. Furthermore, Ir is a fcc metal and, therefore, each bulk atom has a coordination number of 12, i.e., number of nearest neighboring atoms, as can be determined by repeating the fcc unit cells shown in the Fig. 5(a).

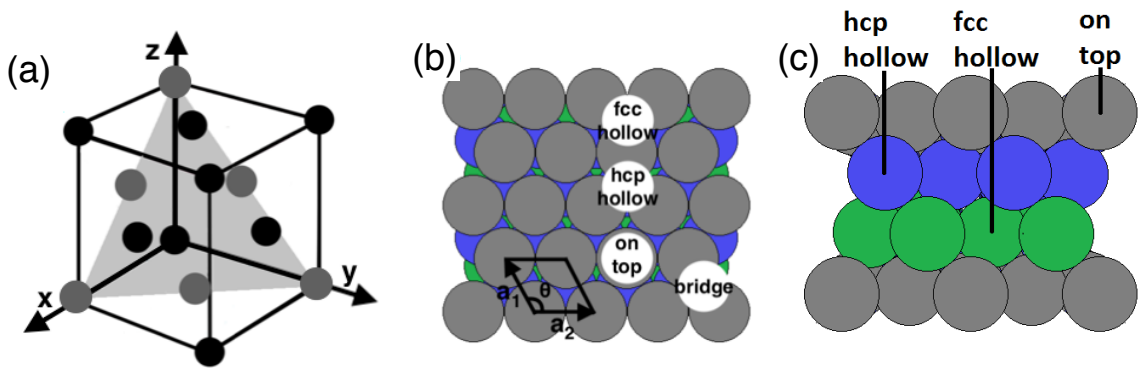

Figure 5: (a) Fcc unit cell with the (111) plane indicated by the transparent gray plane. (b) The ABC stacking of fcc [111] direction, with hexagonal surface unit cell marked by the black rhombus and the high symmetry adsorption sites are also highlighted. (c) Side view of the ABC stacking and the corresponding high symmetry sites.

To create a well defined surface for the growth of Gr/hBN, the iridium single crystal has been cleaved in the [111] direction given by the Miller indices, indicated by the transparent gray plane in the Fig. 5(a). Figure 5(b) shows the Ir(111) dense packed six-fold rotational symmetric surface layer, the symmetry that is preferred for the growth of honeycomb structures. Indicated in the Fig. is also the hexagonal primitive unit cell, with lattice vectors of equal lengths $|\mathbf{a}_1| = |\mathbf{a}_2|$ and an angle of $\theta = 120°$ between them. Important for the characterization of overlayer structures formed on this surface, are the high symmetry adsorption sites, indicated by a three-fold hollow hcp and fcc site, a bridge site and a top site. In Fig. 5(c) the difference between the hcp and fcc hollow adsorption sites is visualized by the ...ABCABC... stacking order of the atomic layers in the fcc(111) direction. The hcp-hollow site has an atom directly below in the second layer, while fcc-hollow site has an atom directly below in the third layer. As a consequence of these two distinct high-symmetry sites, the surface combined with the substrate reduces to three-fold rotational symmetry.

As the Ir crystal is cleaved and the (111) surface is formed, the coordination number for a surface atom is reduced to 9, given by six in-plane nearest neighbors and three below. Consequently, three dangling bonds per surface atom are created, which gives the system surface energy. The surface energy which is partly linked to the catalytic activity of the Ir(111) surface, and is of fundamental importance for dissociating the precursor molecules for growth of the hBN monolayer atop, as will be discussed in the next section. Lastly, it is worth mentioning, that due to the dense packing of the Ir(111) surface, it has lower surface energy than Ir(100) or Ir(110) planes, in the respective increasing order. However, on the upside of this, it will experience less surface relaxation, both in-plane and vertical. Hence, the nearest neighbor distance in the iridium bulk is referenced close to the Ir(111) surface lattice constant with value of $a_{Ir} = 2.7147$ Å at RT [24].

4.2 Structure and Growth of hBN/Ir(111)

By chemical vapor deposition of 100 L of precursor molecule borazine, $B_3H_6N_3$, on a Ir(111) surface kept at 1250 K, only single atomic layer of hBN can be grown as a result of self-termination of the growth process. Figure 6(a) shows an overview STM topograph of the grown hBN monolayer film with these parameters. As seen from the image, the hBN monolayer continues over several underlying Ir(111) step edges without any visible domain boundaries. Furthermore, only a single rotational domain of the STM observed 6-fold symmetric hBN/Ir(111) moiré structure can be verified by the six sharp spots in the fast Fourier transform (FFT), shown as an inset. This moiré structure, with uniform periodicity, originating as a result of the mismatch between the lattice constants of Ir(111), $a_{Ir} = 2.715$ and hBN, (vdW bulk value), $a_{hBN} = 2.504$ Å [25].

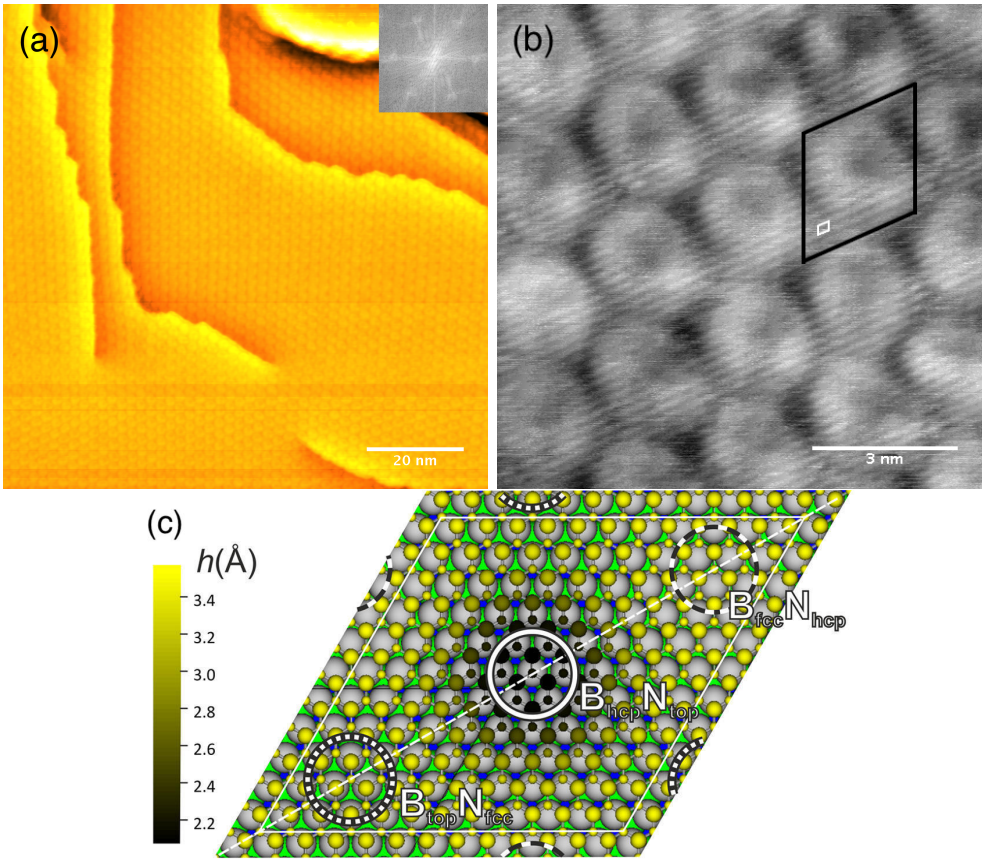

Figure 6: STM and DFT characterization of the real space structure of hBN/Ir(111). (a) 100x100 nm^2 STM overview of the CVD grown hBN/Ir(111), inset: FFT of the STM image. (b) 10x10 nm^2 partial atomic resolution STM topograph, with the moiré and hBN unit cells indicated by the black and white rhombuses, respectively. (c) DFT ball model of a commensurate 12-on-11 hBN/Ir(111) superstructure [26]. Large and small yellow balls indicating the B and N atoms, respectively, (heights, relative to the Ir(111) substrate color coded respect the side bar). Gray, green and blue indicate the Ir atoms in the first second and third layer, respectively.

Figure 6(b) shows a zoom-in of the hBN/Ir(111) moire structure, with partial atomic resolution of the hBN atomic rows in one direction, visible as the lines diagonally across

the image. The translational symmetry of the moiré structure is shown by the moiré unit cell indicated by the black rhombus, while the smaller white is the hBN unit cell. The two unit cells can be said to be aligned to a good approximation. Furthermore, due to the hexagonal nature of the moire structure, the Ir(111) unit cell can be concluded to be aligned with the hBN unit cell as well. Direct measurement of the unit cell lengths yields too small values due to calibration of the piezos and, therefore, are not presented. However, the periodicity of the hBN atomic rows occurring along each moiré unit cell length is carefully measured to give an average of 12 hBN unit cells. The condition for the appearance of the periodic moiré structure, just as in the case of periodic interference pattern, can be described by $r \times r$ hBN unit cells on top of $(r-1) \times (r-1)$ Ir(111) unit cells, provided by their alignment and relative lattice constants. This would then result, as determined directly from the STM topograph, a moiré superstructure of 12×12 hBN unit cells on top of 11×11 Ir(111) unit cells, further referred as 12-on-11. This value would justify the choice of best commensurate superstructure for a DFT simulation seen in Fig. 6(c). A more precise moiré analysis is done in the next section.

As already visible in the STM topograph, Fig. 6(b), the STM does not image the hBN/Ir(111) surface uniformly due to periodic variations of LDOS and/or surface height within the moiré unit cell. So-called pore sites with central depressions appear surrounded by wire sites, named on the account of the discovery [3]. The variation in the LDOS and the surface height can be determined as consequence of different hBN adsorption sites, as determined by the relaxed and most energetically favored hBN overlayer structure in the DFT simulation, Fig. 6(c). The figure highlights three different high-symmetry adsorption sites for boron and nitrogen atoms within the moire cell, reducing the STM observed rotational symmetry to 3-fold. Furthermore, a high corrugation of the overlayer structure is noted with a peak-to-peak amplitude of 1.5 Å across the moiré cell. The lowest lying adsorption site is determined as BN occupying BN(hcp,top), and is attracted close to the substrate due to nitrogen atoms forming a bond with iridium atoms [26], most likely sp^3 hybridizing directly atop. This chemisorbed site is surrounded by two physisorbed sites at increasing heights from the substrate, namely, BN(top,fcc) and BN(fcc,hcp), respectively.

4.2.1 Moiré Analysis

For more precise characterization of the hBN/Ir(111) moiré structure than just a direct measurement on the STM image, one can average and observe the periodicities of the recorded STM image in the reciprocal space by using FFT. Advantageously, the same set of equations for the characterization of the moiré structure in LEED images can be used as well, as was noted in the theory section. Figures 7(a) and (b) show FFT of the partial atomic resolution STM image, Fig. 6(b), and a LEED image of the hBN/Ir(111) structure, respectively. The moiré structure with large real space unit cell results in satellite spots around the labeled Ir(1,0) and hBN(1,0) spots. Due to the very nature of the satellite spots, they can be described as a linear combination of the Ir(111), $\mathbf{a}_i^*$, and hBN, $\mathbf{b}_i^*$, reciprocal lattice vectors as,

$$\boldsymbol{G}_{moire} = n\boldsymbol{a}_1^* + m\boldsymbol{a}_2^* + h\boldsymbol{b}_1^* + k\boldsymbol{b}_2^* \tag{14}$$

An example is given for the moiré spot m(2,0,-1,0) in Fig. 7(b). Furthermore, it is observed from the LEED, that the hBN/Ir(111) structure indeed shows a 3-fold rotational symmetry. This can be seen by following the outer hBN hexagon, and noting that every second hBN spot is of the same intensity, implying that the hexagon can be rotated repeatedly by 120 degrees without affecting it, i.e., 3-fold symmetry. Same argument applies to the Ir(111) spots. It is also clear from the LEED, that the hBN and Ir(111) lattice vectors are aligned quite well.

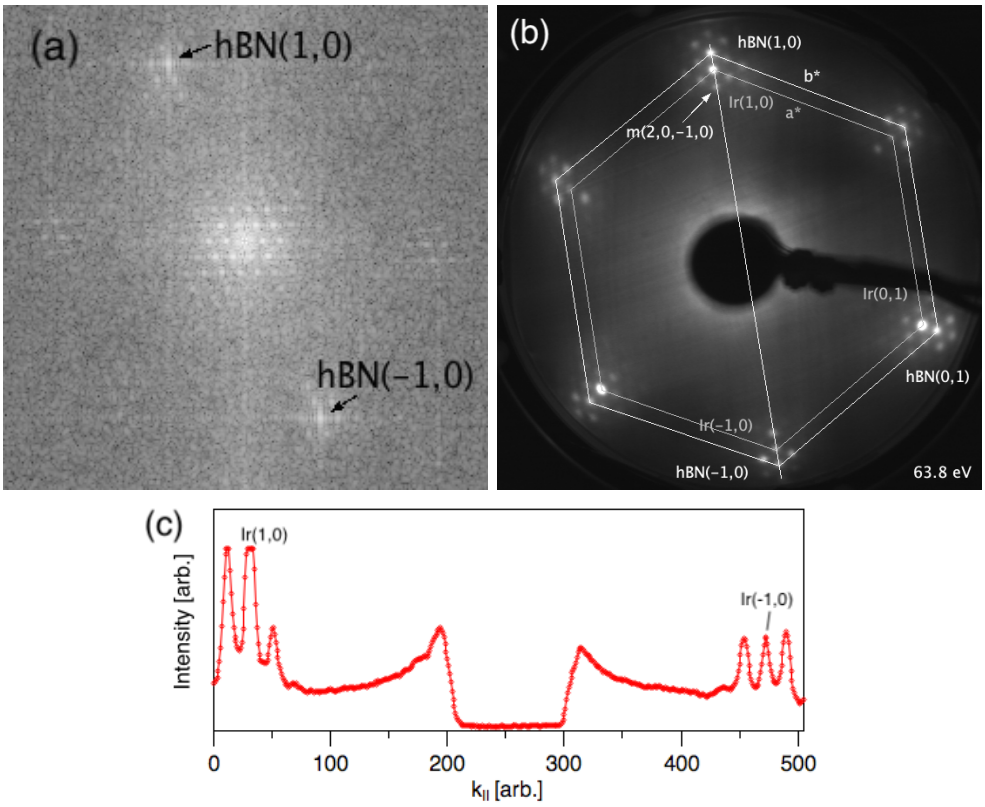

Figure 7: Reciprocal space characterization of hBN/Ir(111) (a) FFT of Fig. 6(b), with the hBN principal spots highlighted by the arrows and rest of the spots originating from the moiré structure. (b) LEED image of hBN/Ir(111). Reciprocal lattice vectors denoted by the principal spots, 63.8 eV electron kinetic energy. (c) Line profile of (b) along $[\bar{1}0\bar{1}0]$ direction.

For the more precise moiré analysis[27], the equation below can be used for both, FFT and LEED.

$$\boldsymbol{k}_{moire} = \boldsymbol{k}_{hBN} - \boldsymbol{k}_{Ir} = \frac{1}{r}\boldsymbol{k}_{hBN} \tag{15}$$

where $\boldsymbol{k}_i$ are the diffracted wavevectors, i.e., the reciprocal lattice vectors and r is the moiré periodicity, fulfilling the previously described real space moiré condition $r \cdot \boldsymbol{a}_{hBN} = (r-1) \cdot \boldsymbol{a}_{Ir}$. Equation (15) further simplifies to a scalar equation as the lattice vectors are aligned. For the FFT in Fig. 7(a), a line profile is measured in the hBN $[\bar{1}0]$-direction and an intensity profile similar to the one in Fig. 7(c), corresponding to LEED $[\bar{1}0\bar{1}0]$ direction, is obtained. Fitting Gaussians to the peaks of the hBN principal and the surrounding six-fold satellite spots representing the moiré periodicity, the lengths of the reciprocal lattice vectors, in arbitrary units, are determined. Using Eq. (15), periodicity of the

hBN unit cells within the moiré cell is calculated as $r = 12.15 \pm 0.28$, again justifying the best commensurate structure of 12-on-11. With value $a_{Ir} = 2.715$ Å, the moiré and hBN lattice constants are determined as, $a_m = 30.28 \pm 0.7$ Å and $a_{hBN} = 2.491 \pm 0.081$ Å.

Similarly, the LEED analysis gives periodicity of $r = 13.10 \pm 0.076$ and, therefore, $a_m = 32.87 \pm 0.19$ Å and $a_{hBN} = 2.508 \pm 0.090$ Å. While the two different moiré periodicities determined by FFT and LEED for the same structure might seem controversial, they are, however, in full agreement with the hBN/Ir(111) superstructures within the literature. That is, Farwick zum Hagen et al.[26] determined a 11.7-on-10.7 superstructure by STM moiré analysis, while a commensurate superstructure of 13-on-12 was determined by LEED study of Orlando et al.[28]. This difference can be accounted for LEED being a macroscopic technique, as the electron beam diameter is usually in the order of mm, while the STM scans are typically in the order of nm^2. Therefore, slightly different moiré domains can be expected to be probed with LEED. The variations of these aligned domains can be explained by the differences in thermal expansions between Ir and hBN at the high CVD dosing temperature, resulting in a compressive stress by a terrace locking effect for terraces of different sizes as the system cools down, which is discussed more in the next section. However, one can note that LEED as a technique assumes flat surfaces, provided by the curved fluorescent screen, therefore, scattering from corrugated hBN overlayer respect to flat Ir(111) can cause minor discrepancies in the determined periodicities with this technique. Nevertheless, to the authors best knowledge, the hBN/Ir(111) moiré structure is generally treated as a 12-on-11 superstructure, based on the recent moiré analysis of zum Hagen et al.[26].

Another disagreement in the structure is, of course, the corrugation. Only on the basis of DFT, Schulz et al.[18] determined a corrugation of 0.35 Å for a 13-on-12 commensurate superstructure, which is in the order of corrugation of Gr on Ir(111)[29]. Interestingly enough, it was determined by Seitsonen et al.[30], that the corrugation of the DFT relaxed structure is not as a result of the best commensurate superstructure chosen, but rather the chosen exchange-correlation functional, treating the many-body interaction in the partly chemisorbed and physisorbed hBN layer on the Ir(111) substrate. However, on the basis of experimental studies of both zum Hagen et al.[26] and Seitsonen et al.[30], the corrugation has been determined as 1.55 Å and 1.65 Å, respectively. This high corrugation of hBN on Ir(111) will definitely affect its properties for growing the Gr/hBN/Ir(111) heterostructure as opposed to the opposite system, hBN/Gr/Ir(111).

4.2.2 Comparison to Gr/Ir(111)

For a better context to the above discussed hBN/Ir(111), it is worthwhile to review the structure and growth of Gr/Ir(111). The experimental data presented here are previous results in the group obtained by V. Boix for her master's thesis[1], unless otherwise stated.

As in the case of hBN/Ir(111), it is an advantage to use the catalytic activity of the Ir surface, therefore, with a precursor molecule, such as ethylene, C_2H_4, Gr can be grown. However, the growth temperature required to achieve a high quality monolayer of Gr, i.e., a single aligned R0 domain, is too high to be efficiently reached with CVD only. This is because ethylene is a small molecule, as opposed to borazine, and, therefore, with a small

sticking coefficient most of it would just immediately desorb from the Ir(111) surface at the required growth temperature. The Gr growth has to be initiated by temperature programmed growth (TPG). In this technique the precursor is dosed at RT followed by step-wise annealing up to 1370 K. To efficiently reach the full monolayer coverage, the growth is complemented by CVD. More in depth discussion of the Gr growth can be found in [1,31].

Figure 8(a) shows a 100×100 nm^2 STM topograph of an aligned monolayer of Gr on Ir(111) extending over several underlying Ir(111) step edges. The six bright spots in the FFT indicate a high quality single domain of the STM observed six-fold symmetric moiré. In Fig. 8(b) is shown an atomic resolution close up of this moiré structure.

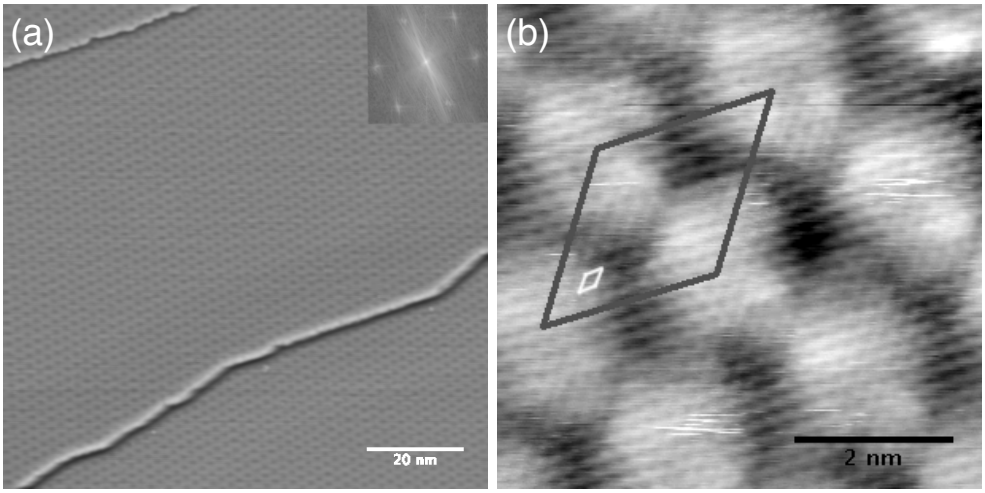

Figure 8: STM characterization of Gr/Ir(111). (a) 100×100 nm^2 overview of the moiré structure. Inset showing the corresponding FFT. (b) 5×5 nm^2 atomically resolved STM with the moiré cell indicated by the black rhombus and the Gr unit cell by the white rhombus. Measured by V. Boix.

Characteristic to a lattice mismatched system, Gr on Ir(111) forms also a moiré structure, looking almost identical to the moiré of hBN/Ir(111). Theoretical moiré periodicity, neglecting any interactions with the substrate, can be directly determined from the mismatch of the Ir(111) lattice constant and the surface lattice constant of bulk graphite, $a_{Gr} = 2.459$ Å [32]. Using the moire condition for an aligned system, as described in previous section; $r \cdot a_{Gr} = (r-1) \cdot a_{Ir}$, and rearranging gives a periodicity of 10.61-on-9.61 Gr unit cells on Ir(111) unit cells. However, based on the moiré analysis of N'Diaye et al. [27], it is generally established that the moiré periodicity of Gr/Ir(111) is 10.32-on-9.32. This deviation from the theoretical value can be used to calculate a compressive stress of approximately 3% within the moiré cell.

In Fig. 9 is shown DFT simulated ball model of 10-on-9 commensurate moiré superstructure of Gr atop Ir(111), with the high symmetry adsorption sites of the C atoms indicated. The optimized Gr overlayer structure is determined to give a peak-to-peak corrugation amplitude of 0.41 Å between the top and the hcp sites, in agreement with the authors experimental values [29].

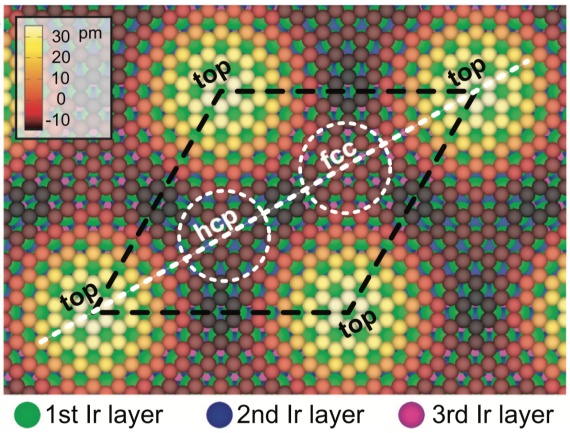

Figure 9: DFT ball model of 10-on-9 commensurate Gr/Ir(111) superstructure [29].

The fcc high symmetry site is determined just slightly higher than the hcp. It is important to note, that the fundamental difference between hBN/Ir(111) and Gr/Ir(111) is not only the larger corrugation of hBN, but also its pronounced pore-wire structure as opposed to the Gr's low lying hcp and fcc "valley-site" within the moiré cell on Ir(111).

Similar observation between the theoretical and experimental moiré periodicity can also be made for hBN on Ir(111). A comparison of the values determined in the previous section to the values of hBN in the vdW bonded bulk, $a_{hBN} = 2.504$ Å [25], reveals a compressive stress of approximately 6% within the moiré cell. For the the two isostructural hexagonal sp^2 hybridized systems, these two percentages could be ultimately related to bond length changes, in the simple picture of an interatomic potential, therefore, indicating a stronger interaction of hBN with the Ir(111) substrate than for Gr on Ir(111).

Negligible amount of the determined compressive stress can be accounted to the larger corrugation of hBN/Ir(111), whereas a large portion can be accounted to the high temperatures used in the growth techniques. hBN has just slightly higher thermal expansion coefficient than Gr, but they are both still very close to zero at 1350 K [33] and, therefore, they can both be neglected respect to iridium's thermal expansion coefficient, $\alpha = 9.78 \cdot 10^{-6}$ K^{-1} [24]. Because of this, at high temperature an Ir terrace will be filled with more hBN or Gr than would be possible at RT. As the system cools down, Ir will exert a force to the hBN or Gr provided by the Ir step edge and the strong binding to the edge atoms as a consequence of their increased amount of dangling bonds, i.e., the previously mentioned terrace locking effect. However, in comparison between hBN and Gr on Ir(111), this effect cancels out or even favors hBN due its slightly higher thermal expansion. Based on this analysis, it can be suggested that the hBN is more strongly bound to Ir(111) and, therefore, the energetically favored stacking order should be Gr atop hBN/Ir(111).

Finally, it is to be concluded, that due to the three distinct high symmetry adsorption sites of Gr/Ir(111) reducing the STM observed 6-fold symmetry to 3-fold symmetry, a LEED image almost identical to hBN/Ir(111) is to be expected. With the only difference being the relative mismatch of the lattice constants of 1.8 % between hBN and Gr, or more precisely, the small difference in the periodicities of the moiré structures, 13-on-12 and 10-on-9. Therefore, combined with an almost identical looking moiré structure in

the STM images, the distinction between possibly different domains of hBN and Gr on Ir(111) based only on their structures has to precise.

4.3 Structure and Growth of Gr/hBN/Ir(111)

Due to the inertness of the monolayer hBN on Ir(111), nothing is going to happen by directly dosing ethylene on top of it. To circumvent the limitation caused by the catalytically active Ir(111) substrate being fully covered, i.e., to dissociate the ethylene for the Gr growth, the electron assisted growth technique (EAG) will come in to use. In this technique, an electron shower from a filament is used to dissociate the ethylene molecule already at RT. The dosing at RT is then followed by step-wise annealing, similar to temperature programmed growth (TPG), and possibly Gr can form; leading to the electron assisted growth of the heterostructure of Gr atop hBN/Ir(111).

Below is shown an overview of STM and LEED images recorded after RT dosing of ethylene in the electron shower, followed by subsequent annealing to different temperatures. Two ethylene dosages and different annealing steps are presented, namely: Dose 300 L at RT and anneal in steps of; 773 K, 1073 K and 1273 K – start over with clean hBN/Ir(111) and dose 6000 L at RT, followed by annealing in steps of; 773 K, 973 K, 1173 K, 1373 K.

Figure 10(a) shows a clean, high quality hBN overlayer extending over several Ir(111) step edges before dosing the ethylene. In Fig 10(b) is shown the system after dosing 6000 L of ethylene on top of hBN at RT, (no good quality image for the 300 L dose were possible due to the STM tip picking up too many weakly bound radicals). From the figure it is immediately evident that the sticking coefficient of ethylene on top of hBN/Ir(111) is very small, as a dose of 6000 L of ethylene yields only partial coverages, in comparison to the full hBN monolayer growth directly on Ir(111) with only 100 L borazine. Figure 10(c) is recorded after annealing the 300 L dose at 1073 K, where it is visible how less, but bigger clusters are formed, occupying mainly the edge sites of the hBN/Ir(111). This is because at low annealing temperatures the molecules gain kinetic energy and diffuse around the surface, decaying when the cluster size is big enough. Furthermore, the clusters tend to favor the edge sites due to the strong binding to edge atoms, again as a consequence of their increased amount of dangling bonds.

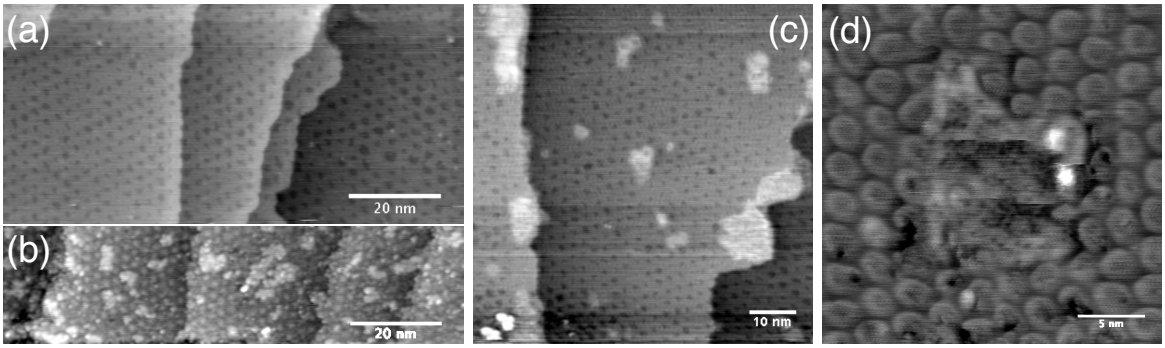

Figure 10: (a) Clean hBN/Ir(111) (b) 6000 L dose at RT (c) 300 L dose after annealing at 1073 K (d) Zoom-in on a cluster of 300 L dose after annealing at 1073 K.

In Fig. 10(d) is shown a high resolution close up of a carbon cluster for the 300 L dose after annealing at 1073 K. The cluster is determined to have some signs of periodicity, however, different from the common moiré structure. Additionally, the hBN low lying pore and the surrounding wire structure is clearly visible.

For a comparison, a similar set of STM and LEED images for the 6000 L dose of ethylene and subsequent annealing is shown below. Figures 11(a) and (b) show STM topographs after the annealing steps of 773 K and 1173 K, respectively. The STM images clearly show the same cluster formation as for the 300 L dose, but naturally at increased amounts. In Fig. 11(c) is shown a LEED image of (b), where the satellite spots due to the moiré structure of hBN are visible and no diffraction spots can be observed due to the clusters. This LEED image can also be qualitatively referenced for all the previous figures, i.e., no diffraction spots were observed due to the clusters at any of the previous annealing steps. However, this LEED cannot be referenced for Fig. 11(a), which will be discussed in Sec. 4.3.1.

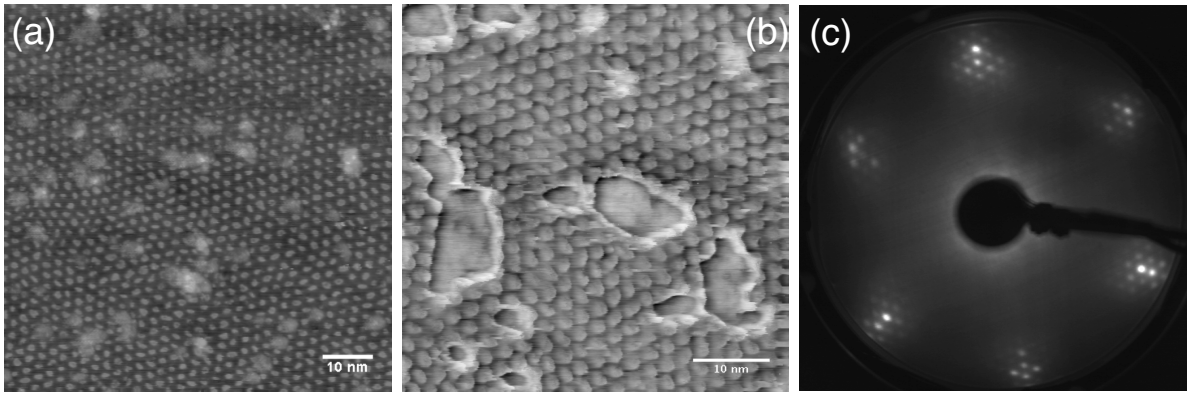

Figure 11: (a) 6000 L dose after annealing at 773 K (b) 6000 L dose after annealing at 1173 K (c) LEED of (b), 63.8 eV.

By following the moiré structure vertically from the top of the Fig. 11(a), it is also visible that it is rather wavy. This could be interpreted as the clusters being intercalated below the hBN layer and, therefore, bending the hBN layer. Furthermore, after the annealing step of 773 K, the moiré structure itself looks very different compared to all the previously acquired STM images, with very strong tunneling coming from the hBN pore sites. Moreover, the "pores" are clearly varying in sizes, orientations and have rather cluster like shapes with sharp edges. A more familiar moiré structure is again observed after annealing at 1173 K, as shown in Fig. 11(b).

Finally, it is to compare the high temperature annealing steps of the both doses; (300 L)-(1273 K) and (6000 L)-(1373 K), shown in Figs. 12(a) and (b-c), respectively. In the top right corner of Fig. 12(a), a bare patch of Ir(111) is visible with white dots being pre-existing impurities. This area has probably never been covered by hBN and no carbon clusters can either be determined after annealing at this high temperature. Furthermore, the moiré structure of hBN has clearly started breaking, most likely due to the high thermal expansion of the Ir(111) substrate. The hBN layer is seen to form flakes of characteristic triangular shape, as a consequence of highly energetically favored boron termination of the hBN edge[26].

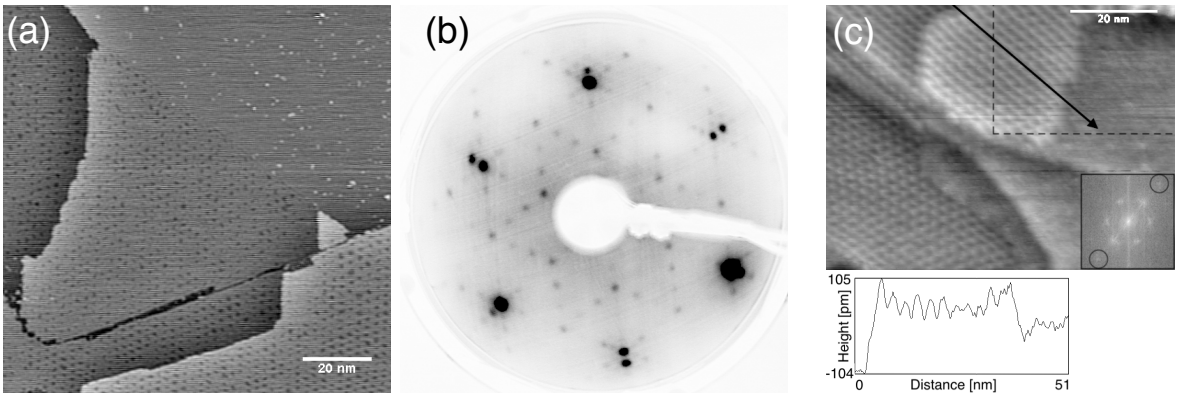

Figure 12: (a) After annealing the 300 L dose at 1273 K (b) 81.4 eV LEED of (c) with contrast inverted for visibility. (c) 6000 L dose after annealing at 1373 K, corresponding FFT as an inset, where black circles highlight newly observed spots. Below, a line scan of the apparent height along the black solid arrow.

Now the interesting part, namely, what are the completely new periodicities observed in the LEED pattern, Fig. 12(b), recorded after annealing the 6000 L dose at 1373 K. From the corresponding STM image, Fig. 12(c), a moiré structure is clearly visible. This can be immediately accounted for the satellite spots around the very bright Ir(111) substrate spots. However, with clear differences to the moiré structure and non-triangular domain shapes, as observed in Fig. 12(a), combined with the high 6000 L dose, this moiré cannot be directly accounted to hBN. Inside the black dashed box in Fig. 12(c), a phase showing periodicity is clearly observed. This area can definitely be accounted for some of the new diffraction spots. In particular, from the FFT a periodicity of approximately half of the moiré structure in real space can be determined, denoted by the faint spots inside the black circles. Zoom-in and a better resolution FFT of the dashed box area will be discussed in Sec. 4.3.2.

At the very beginning of the line scan along the line indicated by the black arrow in Fig. 12(c), there is a clear height difference between the two, lower and upper moirés. In the STM image, the transition between these two moirés looks rather continuous, as opposed to an abrupt which would be the case if there was an underlying Ir(111) step edge. Therefore, they could be the same layer, but with something intercalated giving a lift to part of the moiré. Furthermore, if there is something intercalated and the two moirés are on the same substrate terrace, the periodic phase at the end of the line scan cannot be Ir(111) because it is higher than the lowest moiré at the beginning of the line scan. On the basis of intercalation at this large scale, resulting in an uniform lift of the moiré structure, it would most likely be crystalline. However, it has already been suggested by the structural comparison between Gr and hBN on Ir(111) in Sec. 4.2.2, that the most energetically favored stacking order should be Gr atop hBN on Ir(111). This is further confirmed by DFT simulations of zum Hagen et al.[26], which gave binding energies per atom for Gr; $E_b = -69.0$ meV and for hBN; $E_b = -86.8$ meV. This new structure will be fully characterized in Sec. 4.3.2.

4.3.1 Nanotemplate - Charging of the Substrate

For the growth of vertical vdW heterostructure, a flat substrate is naturally preferred. Even for the slightly corrugated hill-valley structure of Gr on Ir(111), so-called nanotemplating effects are well known and studied [34]. Nanotemplating, enabling to periodically trap atoms, ions, molecules or clusters to the moiré structure due to the periodic variations in its structure and properties. This effect is even more important for the highly corrugated and pronounced pore-wire structure of hBN/Ir(111), as discussed in Sec. 4.2.2. In particular, it has been studied by Schulz et al. [18], that in addition to the high geometric corrugation, the hBN/Ir(111) structure also has a work function modulation of 0.5 eV between the pore and wire sites. This work function modulation imposes strong lateral electric fields, so-called dipole rings, across the surface, which can then result in trapping to the pore sites of hBN/Ir(111) [35]. Therefore, as attempting to grow Gr atop hBN/Ir(111), it is important to consider the possibility of site-selective adsorption.

As mentioned in the overview Fig. 11(a), the highly varied STM imaging conditions and the cluster like shapes, could be consequence of carbon clusters adsorbing to the low lying pore sites. Below are shown, a STM image and the corresponding highly attenuated LEED, acquired after annealing the 6000 L ethlyne dose at 773 K.

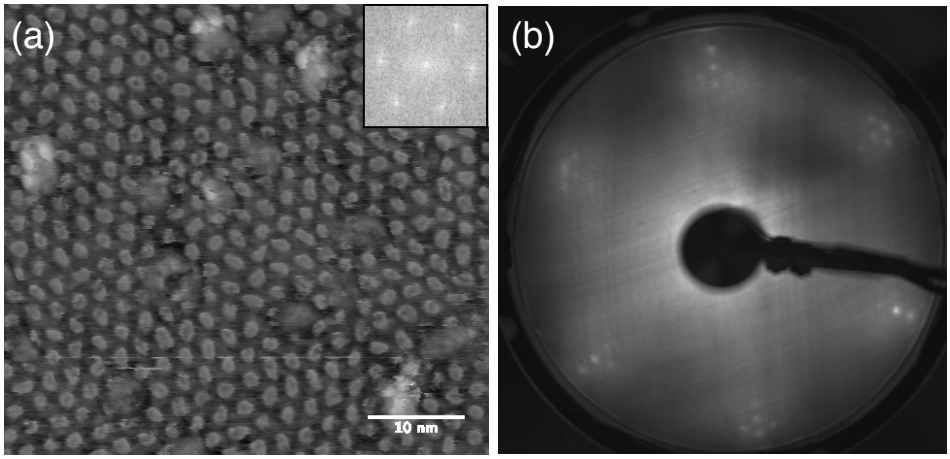

Figure 13: (a) STM image after annealing the 6000 L dose at 773 K. (b) The corresponding LEED, 63.8 eV.

At first sight it is hard to make an argument based on the STM image, as it seems that there is exactly one cluster within every moiré site, i.e., a cluster density of one, and no empty pore sites are visible. From literature it is noted, that most of the previous studies have all had densities well below one, such as templating napthalocyanine molecules on the even more corrugated hBN/Rh(111) [36]. However, in a very recent study by Will et al. [37], the authors succeeded to template a carbon cluster within every moiré cell of hBN/Ir(111). The authors, however, dosed elemental C directly at 400 K and not ethylene at RT followed by annealing at 773 K, as done here. On the account of this, it can be seen in the Fig. 10(b), that dosing 6000 L of ethylene at RT resulted in rather large carbon clusters forming island like metal on metal. Therefore, it seems unlikely that these clusters decomposed and templated perfectly to the pore sites after annealing at

773 K. Furthermore, this templating effect was not observed for the 300 L dose at any of the annealing steps.

Nevertheless, the attenuation of the corresponding LEED in Fig. 13(b), has to be argumented. Clusters being adsorbed to the pore sites, could explain the attenuation of the satellite spots corresponding to the moiré structure. However, due to the inelastic free mean path of low kinetic energy electrons being in the order of few atomic layers, the Ir(111) spots should still be observed. Therefore, and together with the above discussion, it is more reasonable to consider effects of charging the system by the EAG technique. In the 300 L dose, where this effect was not observed, the system was exposed to electrons for 300 s, while the electron exposure was 600 s for the 6000 L dose. As the electron diffraction techniques rely on scattering from Coulomb forces of both the nuclei and the surrounding electron cloud, an uneven charging of the hBN/Ir(111) would cause an attenuation of the diffraction pattern, especially in the case of low kinetic energy electrons. Furthermore, the uneven charging would also explain the STM tunneling conditions and the cluster like shapes of the pore sites, as just local trapped charge tunneling.

The attenuated LEED and the corresponding STM is only observed after annealing at 773 K and the possible charging effect is released at higher annealing steps, as already mentioned in Figs. 11(b) and (c). Furthermore, this charging effect should be observed on hBN/Ir(111) without dosing ethylene.

4.3.2 High Temperature Annealing of Gr/hBN/Ir(111)

It is now left to resolve the new structure after annealing the 6000 L dose at 1373 K, as introduced in the Figs. 12(b-c). At this high annealing temperature and dose, it is not completely clear by just inspection, whether the observed moiré structure corresponds to hBN or Gr. Especially, since it is further known that hBN on Ir(111) starts to heavily decompose around 1300 K, while Gr/Ir(111) is unaffected up to 1500 K, as determined by Usachov et al.[38]. Moreover, this study also shows that when annealing hBN/Ir(111) higher than 1300 K, the intensity of N 1s photoemission peak decreases at a higher rate compared to B 1s from X-ray photoelectron spectra (XPS). Based on this, it could be assumed, that there is a boron superstructure responsible for, at least, some of the new diffraction spots.

Below in Fig. 14(a) is shown a 73.9 eV LEED after the 1373 K annealing of the 6000 L dose. Measuring along the dashed line, corresponding line scan shown in Fig. 14(c), for a perfectly aligned moiré, the moiré structure is determined to have a periodicity of r = 13.09 $\pm$ 0.067 i.e., 13.09-on-12.09. This periodicity is almost identical and within the errors of the moiré periodicity determined from the LEED of the pristine hBN/Ir(111) in Sec. 4.2.1; 13.10-on-12.10. The hBN moiré can now be used as a reference to determine the periodicities of the unknown domains in the STM Figures 14(b) and (d).

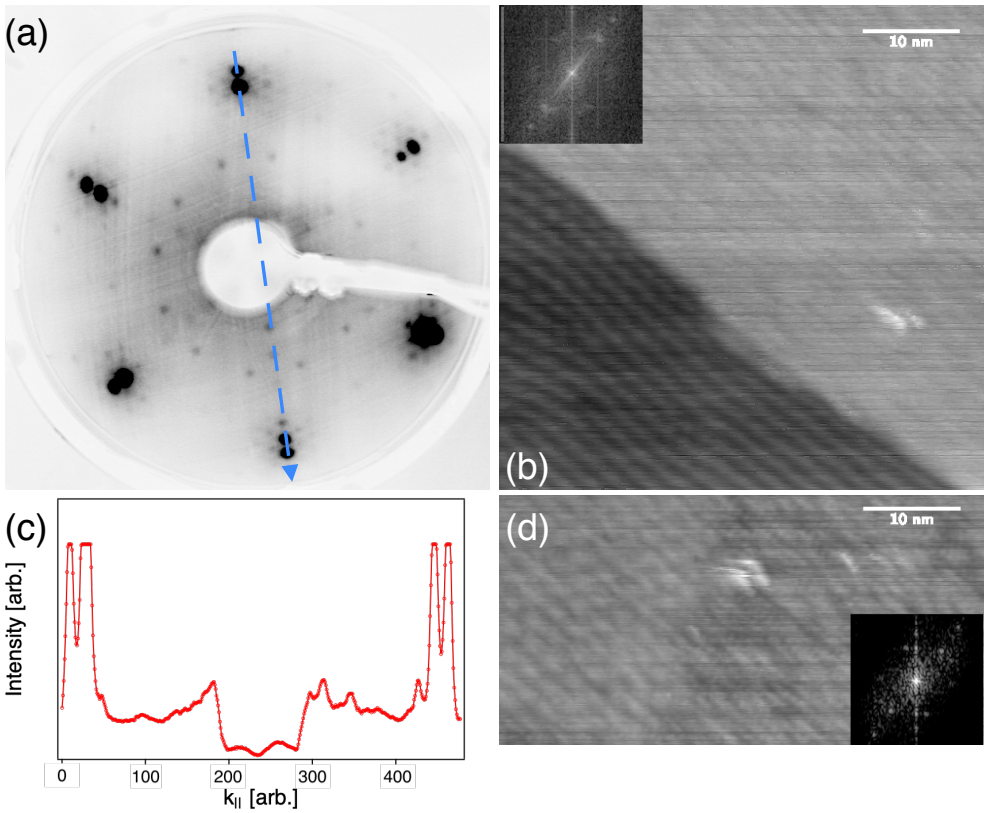

Figure 14: (a) LEED after annealing the 6000 L dose at 1373K, 73.9 eV. (b) STM image of an unknown periodic domain parallel to the moiré (c) Line scan of (a) along the dashed line. (d) STM image of an undetermined periodic domain blending in to the moiré structure, (zoom-in of the black dashed box in the Fig. 12(c)).

Determining the ratio of reciprocal distances of the moiré, d_m, respect to the undetermined domain, d_d, i.e., the ratio of lengths of the moiré spots and the new faint spots in the FFT, (the spot positions were also highlighted by the black circles in the overview, Fig. 12(c), if not visible). Furthermore, multiplying this ratio by the Ir(111) moiré periodicity determined by the STM moiré analysis in the pristine hBN/Ir(111) section, i.e., $[(d_m/d_d)\times$ 11.15] Ir lattice constants. This calculation yielding a superstructure of approximately every six Ir(111) real space lattice constants, aligned with the moiré structure at least in one direction. Therefore, it is aligned with some of the dense packed directions of Ir(111) as well. No other periodic phases can be determined with STM.

The small reciprocal space periodicities, other than the hBN satellite spots, in the LEED image are also determined to give this same periodicity of six. Furthermore, due to the well defined peak profiles of the hBN and moiré peaks in the line scan Fig. 14(c), no R0 aligned domain of Gr can exist, at least in high coverages. Knowing that the moiré corresponds to hBN and observing how the determined domain blends into it in Fig. 14(d) together with the above discussed XPS study of Usachov et al.[38], this six periodic superstructure is now claimed to consist of boron.

Returning back to the 81.4 eV LEED, shown again in Fig. 15(a), and noting that the newly observed high intensity diffraction spots correspond to a rather textbook example of an oxygen phase on fcc(111), i.e., a (2×1)-O superstructure. The structure which,

however, cannot be distinguished from a (2 × 2) superstructure as already described within the theory section of LEED, Figs. 3(a-b). Combining this with the determined six periodicity in some dense packed directions of Ir(111), it can now be argumented that: All the new diffraction spots can be explained by (6×2)-B superstructure with three coexisting rotational domains, rotated by 120° respect to each other.

Figure 15(b) shows schematic LEED pattern of a (6×2) superstructure on fcc(111), where the three colors indicate the three different rotational domains. The observation of the bright (2×1) spots in the experimental LEED can be further justified by the coinciding of all three rotational domains, shown by the smaller white spots in Fig. 15(b).

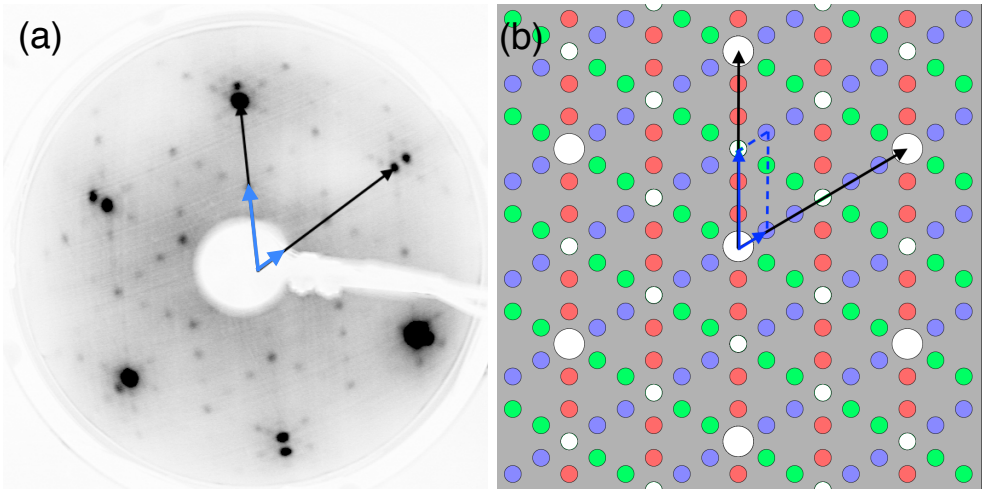

Figure 15: (a) LEED of hBN/Ir(111) and three coexisting rotational domains (6 × 2)-B superstructures, 81.4 eV. (b) Schematic LEED pattern of three rotational domains of (6 × 2) superstructures on fcc(111), from [16].

It can now be concluded, that the rather challenging looking LEED can be explained by hBN moiré on Ir(111) and three coexisting rotational domains (6 × 2)-B superstructures, as a consequence of hBN decomposing and nitrogen desorbing leaving boron behind. However, the (6×2)-B structure has a density of almost 8 times less compared to the boron atoms in hBN, therefore, vast amount of boron has also either desorbed or segregated in to the Ir(111) crystal. Furthermore, this (6×2)-B superstructure, also known as the boron nanoribbons, is often observed in high temperature annealing of hBN/Ir(111) [38–40], and even in the high temperature annealing of the opposite system, i.e., after dosing borazine on Gr/Ir(111) [1]. However, often atomic resolution STM images of the boron nanoribbons are obtained, see e.g. [1]. The poor quality of the boron nanoribbons observed here could be explained by possible carbon sub-structures inside the loose unit cell of the boron nanoribbons. This would further explain why some of the diffraction spots are never observed in any of the recorded LEED images as a consequence of multiple scattering. Lastly, on the account of the intercalated domain mentioned in the overview Fig. 12(c) and possible superposition of diffraction spots, it is noted, that the observed LEED pattern cannot represent any Gr rotational domains on Ir(111) [41].

5 Conclusion

In summary, the moiré structure of CVD grown single-domain hBN/Ir(111) has been characterized by both STM moiré and LEED analysis. This analysis revealed two different moiré structures of 12.15-on-11.15 and 13.10-on-12.10, respectively, in full agreement with the literature. Even though the moiré structures of both hBN and Gr were observed to be very similar on Ir(111), the variations of the lateral atomic registries within the moiré cell combined with the distinguishable two atom basis of hBN was determined to give hBN a rather unique, highly corrugated pore-wire structure. Furthermore, by comparing the changes between the bulk lattice constants of hBN and Gr to the values of both on Ir(111) in combination with their relative thermal expansions. It was suggested, that hBN is more strongly bound to the Ir(111) substrate and, therefore, the favored heterostructure stacking order should be Gr atop hBN/Ir(111).

After characterizing and comparing the growth and structure of hBN and Gr atop Ir(111), the temperature evolution of EAG of Gr atop hBN/Ir(111) was discussed for two different ethylene dosages, 300 L and 6000 L. Very small sticking coefficient of ethylene atop hBN/Ir(111) could be immediately noted. Nevertheless, carbon clusters were still achieved on the otherwise inert hBN/Ir(111) with the EAG technique. No Gr formation was observed after any of the annealing steps for the 300 L dose. The 6000 L dose showed a highly attenuated LEED after being annealed at 773 K, with strong cluster shaped tunneling conditions from the hBN pore sites in the STM image. Possibility of nanotemplating carbon clusters to the pore sites were discussed. However, the cluster shaped tunneling conditions and the attenuated LEED could be more plausibly explained by an uneven charging of the substrate by the electron beam used in the EAG technique.

After annealing the 6000 L dose at 1373 K, new periodicities were observed in the LEED pattern. The hBN moiré was directly determined from the LEED. Studying the periodic domains in STM images by FFT, it was determined that the new LEED pattern is entirely described by three coexisting rotational domains of (6×2) boron nanoribbon superstructures. This superstructure is a consequence of hBN decomposing and nitrogen desorbing leaving boron behind. No Gr formation was observed for the 6000 L dose either.

In conclusion for the heterostructure growth, the electron assisted growth technique has now been characterized for both growth orders of Gr/hBN/Ir(111) and hBN/Gr/Ir(111) [1]. The latter order is concluded to yield better results. This can mainly be accounted to: Higher thermal stability of the less corrugated Gr/Ir(111), higher sticking coeffiecient of borazine atop Gr/Ir(111) and the easier growth of the stronger binding hBN on Ir(111). However, the high corrugation and the chemisorbed pore sites of hBN/Ir(111) gives potential for future applications with and without the EAG technique.

6 Outlook

The present study focused on the structural characterization of the phases formed upon dosing ethylene atop hBN/Ir(111) in an electron shower. An obvious extension of this work would be chemical analysis. Ultraviolet photoelectron spectroscopy could be, for example, used to probe the σ-band splitting for hBN/Ir(111) as a result of the chemisorbed pores

and the surrounding physisorbed wires. In such studies, it would be easy to probe possible site-selective adsorption to the pore sites by an attenuation of the corresponding peak. Another technique that could be interesting to use on the Gr/hBN/Ir(111) system is XPS. In contrast to LEED and STM characterization, such studies could answer whether or not the carbon fully desorbs upon annealing to 1373 K.

Even though the favored stacking order should be Gr atop hBN/Ir(111), one problem that my studies revealed is the decomposition of hBN below the high quality Gr growth temperature at approximately 1400 K. Further limitations can be caused by the corrugation. An interesting future direction of my research project could, therefore, be to try to grow the heterostructure of Gr atop hBN on a substrate that is not strongly interacting, given in the increasing order of the corrugation: Ni(111)-Cu(111)-Pt(111)-Ir(111)-Rh(111)-Ru(0001) [5, 42].

As already mentioned, the corrugation and, therefore, the possible templating effects are, however, what makes the hBN such an intriguing 2DM. And, if it was correct that the electron beam in the EAG technique can charge the hBN/Ir(111) surface around the pore sites, hence, making the hBN/Ir(111) a suitable charged template for ions, applications are endless, most notably in the field of quantum computing. Therefore, another interesting research direction would be to do proper characterization of the charging effect. For example, by just exposing the hBN/Ir(111) to electrons without dosing ethylene and recording LEED and STM images for a more precise characterization of the temperature evolution.

References

[1] V. Boix De La Cruz, "Electron assisted growth of h-bn on gr/ir(111)," 2018, student Paper. [Online]. Available: http://lup.lub.lu.se/student-papers/record/8955893

[2] K. S. Novoselov, A. K. Geim, S. V. Morozov, D. Jiang, Y. Zhang, S. V. Dubonos, I. V. Grigorieva, and A. A. Firsov, "Electric field effect in atomically thin carbon films," *Science*, vol. 306, no. 5696, pp. 666–669, 2004. [Online]. Available: http://science.sciencemag.org/content/306/5696/666

[3] M. Corso, W. Auwärter, M. Muntwiler, A. Tamai, T. Greber, and J. Osterwalder, "Boron nitride nanomesh," *Science*, vol. 303, no. 5655, pp. 217–220, 2004. [Online]. Available: http://science.sciencemag.org/content/303/5655/217

[4] R. Laskowski, P. Blaha, T. Gallauner, and K. Schwarz, "Single-layer model of the hexagonal boron nitride nanomesh on the rh(111) surface," *Phys. Rev. Lett.*, vol. 98, p. 106802, Mar 2007. [Online]. Available: https://link.aps.org/doi/10.1103/PhysRevLett.98.106802

[5] A. Preobrajenski, M. Nesterov, M. L. Ng, A. Vinogradov, and N. Mårtensson, "Monolayer h-bn on lattice-mismatched metal surfaces: On the formation of the nanomesh," *Chemical Physics Letters*, vol. 446, no. 1, pp. 119 – 123, 2007. [Online]. Available: http://www.sciencedirect.com/science/article/pii/S0009261407010998

[6] A. H. Castro Neto, F. Guinea, N. M. R. Peres, K. S. Novoselov, and A. K. Geim, "The electronic properties of graphene," *Rev. Mod. Phys.*, vol. 81, pp. 109–162, Jan 2009. [Online]. Available: https://link.aps.org/doi/10.1103/RevModPhys.81.109

[7] J. Wang, F. Ma, and M. Sun, "Graphene, hexagonal boron nitride, and their heterostructures: properties and applications," *RSC Adv.*, vol. 7, pp. 16 801–16 822, 2017. [Online]. Available: http://dx.doi.org/10.1039/C7RA00260B

[8] J. Wang, F. Ma, W. Liang, R. Wang, and M. Sun, "Optical, photonic and optoelectronic properties of graphene, h-bn and their hybrid materials," vol. 6, pp. 943–, 2017. [Online]. Available: https://www.degruyter.com/view/j/nanoph.2017.6.issue-5/nanoph-2017-0015/nanoph-2017-0015.xml

[9] L. Britnell, R. V. Gorbachev, R. Jalil, B. D. Belle, F. Schedin, A. Mishchenko, T. Georgiou, M. I. Katsnelson, L. Eaves, S. V. Morozov, N. M. R. Peres, J. Leist, A. K. Geim, K. S. Novoselov, and L. A. Ponomarenko, "Field-effect tunneling transistor based on vertical graphene heterostructures," *Science*, vol. 335, no. 6071, pp. 947–950, 2012. [Online]. Available: http://science.sciencemag.org/content/335/6071/947

[10] C. R. Dean, A. F. Young, I. Meric, C. Lee, L. Wang, S. Sorgenfrei, K. Watanabe, T. Taniguchi, P. Kim, K. L. Shepard, and J. Hone, "Boron nitride substrates for high-quality graphene electronics," *Nature Nanotechnology*, vol. 5, pp. 722 EP –, 08 2010. [Online]. Available: https://doi.org/10.1038/nnano.2010.172

[11] S. Majety, X. K. Cao, R. Dahal, B. N. Pantha, J. Li, J.-Y. Lin, and H. X. Jiang, "Semiconducting hexagonal boron nitride for deep ultraviolet photonics," *Proceedings of SPIE - The International Society for Optical Engineering*, vol. 8268, pp. 70–, 01 2012.

[12] B. Hunt, J. D. Sanchez-Yamagishi, A. F. Young, M. Yankowitz, B. J. LeRoy, K. Watanabe, T. Taniguchi, P. Moon, M. Koshino, P. Jarillo-Herrero, and R. C. Ashoori, "Massive dirac fermions and hofstadter butterfly in a van der waals heterostructure," *Science*, vol. 340, no. 6139, pp. 1427–1430, 2013. [Online]. Available: http://science.sciencemag.org/content/340/6139/1427

[13] H. Wang, Y. Zhao, Y. Xie, X. Ma, and X. Zhang, "Recent progress in synthesis of two-dimensional hexagonal boron nitride," *Journal of Semiconductors*, vol. 38, no. 3, p. 031003, 2017. [Online]. Available: http://stacks.iop.org/1674-4926/38/i=3/a=031003

[14] P. Hoffman, *Surface Physics: An Introduction*, 2016, ch. 7, pp. 175–176.

[15] H. Ibach, *Physics of Surfaces and Interfaces*. Springer Berlin Heidelberg New York, 2006, ch. 1, pp. 3–4.

[16] K. Hermann and M. A. V. Hove, "Leedpat4," Dec. 2015, [Online; accessed 25-November-2018]. [Online]. Available: http://www.fhi-berlin.mpg.de/KHsoftware/LEEDpat/

[17] G. Binnig, H. Rohrer, C. Gerber, and E. Weibel, "Surface studies by scanning tunneling microscopy," *Phys. Rev. Lett.*, vol. 49, pp. 57–61, Jul 1982. [Online]. Available: https://link.aps.org/doi/10.1103/PhysRevLett.49.57

[18] F. Schulz, R. Drost, S. K. Hämäläinen, T. Demonchaux, A. P. Seitsonen, and P. Liljeroth, "Epitaxial hexagonal boron nitride on ir(111): A work function template," *Phys. Rev. B*, vol. 89, p. 235429, Jun 2014. [Online]. Available: https://link.aps.org/doi/10.1103/PhysRevB.89.235429

[19] J. Tersoff and D. R. Hamann, "Theory of the scanning tunneling microscope," *Phys. Rev. B*, vol. 31, pp. 805–813, Jan 1985. [Online]. Available: https://link.aps.org/doi/10.1103/PhysRevB.31.805

[20] J. Bardeen, "Tunnelling from a many-particle point of view," *Phys. Rev. Lett.*, vol. 6, pp. 57–59, Jan 1961. [Online]. Available: https://link.aps.org/doi/10.1103/PhysRevLett.6.57

[21] C. J. Chen, "Tunneling matrix elements in three-dimensional space: The derivative rule and the sum rule," *Phys. Rev. B*, vol. 42, pp. 8841–8857, Nov 1990. [Online]. Available: https://link.aps.org/doi/10.1103/PhysRevB.42.8841

[22] ——, "Origin of atomic resolution on metal surfaces in scanning tunneling microscopy," *Phys. Rev. Lett.*, vol. 65, pp. 448–451, Jul 1990. [Online]. Available: https://link.aps.org/doi/10.1103/PhysRevLett.65.448

[23] ——, *Introduction to Scanning Tunneling Microscopy*, 2nd ed. Oxford university Press, 2008, ch. 1.

[24] J. W. Arblaster, "Crystallographic Properties of Iridium Assessment of properties from absolute zero to the melting point," *Plat. Met. Rev.*, vol. 54, no. 2, pp. 93–102, Apr 2010.

[25] R. S. Pease, "An X-ray study of boron nitride," *Acta Crystallographica*, vol. 5, no. 3, pp. 356–361, May 1952. [Online]. Available: https://doi.org/10.1107/S0365110X52001064

[26] F. H. Farwick zum Hagen, D. M. Zimmermann, C. C. Silva, C. Schlueter, N. Atodiresei, W. Jolie, A. J. Martínez-Galera, D. Dombrowski, U. A. Schröder, M. Will, P. Lazić, V. Caciuc, S. Blügel, T.-L. Lee, T. Michely, and C. Busse, "Structure and growth of hexagonal boron nitride on ir(111)," *ACS Nano*, vol. 10, no. 12, pp. 11 012–11 026, 2016, pMID: 28024332. [Online]. Available: https://doi.org/10.1021/acsnano.6b05819

[27] A. T. N'Diaye, J. Coraux, T. N. Plasa, C. Busse, and T. Michely, "Structure of epitaxial graphene on ir(111)," *New Journal of Physics*, vol. 10, no. 4, p. 043033, 2008. [Online]. Available: http://stacks.iop.org/1367-2630/10/i=4/a=043033

[28] F. Orlando, R. Larciprete, P. Lacovig, I. Boscarato, A. Baraldi, and S. Lizzit, "Epitaxial growth of hexagonal boron nitride on ir(111)," *The Journal of Physical Chemistry C*, vol. 116, no. 1, pp. 157–164, 2012. [Online]. Available: https://doi.org/10.1021/jp207571n

[29] S. K. Hämäläinen, M. P. Boneschanscher, P. H. Jacobse, I. Swart, K. Pussi, W. Moritz, J. Lahtinen, P. Liljeroth, and J. Sainio, "Structure and local variations of the graphene moiré on ir(111)," *Phys. Rev. B*, vol. 88, p. 201406, Nov 2013. [Online]. Available: https://link.aps.org/doi/10.1103/PhysRevB.88.201406

[30] A. P. Seitsonen, F. Schulz, and P. Liljeroth, "Benchmarking van der Waals-treated DFT: The case of hexagonal boron nitride and graphene on Ir(111)," *ArXiv e-prints*, May 2018.

[31] E. Gråsäs, "Above and below graphene: Nanoparticle chemistry and interface reactions," Ph.D. dissertation, Lund University, 2014. [Online]. Available: http://lup.lub.lu.se/record/4463609

[32] Y. Baskin and L. Meyer, "Lattice constants of graphite at low temperatures," *Phys. Rev.*, vol. 100, pp. 544–544, Oct 1955. [Online]. Available: https://link.aps.org/doi/10.1103/PhysRev.100.544

[33] C. Sevik, "Assessment on lattice thermal properties of two-dimensional honeycomb structures: Graphene, h-bn, h-mos_2, and h-$mose_2$," *Phys. Rev. B*, vol. 89, p. 035422, Jan 2014. [Online]. Available: https://link.aps.org/doi/10.1103/PhysRevB.89.035422

[34] J. Knudsen, P. J. Feibelman, T. Gerber, E. Grånäs, K. Schulte, P. Stratmann, J. N. Andersen, and T. Michely, "Clusters binding to the graphene moiré on ir(111): X-ray photoemission compared to density functional calculations," *Phys. Rev. B*, vol. 85, p. 035407, Jan 2012. [Online]. Available: https://link.aps.org/doi/10.1103/PhysRevB.85.035407

[35] W. Auwärter, "Hexagonal boron nitride monolayers on metal supports: Versatile templates for atoms, molecules and nanostructures," *Surface Science Reports*, pp. –, 2018. [Online]. Available: http://www.sciencedirect.com/science/article/pii/S0167572918300517

[36] S. Berner, M. Corso, R. Widmer, O. Groening, R. Laskowski, P. Blaha, K. Schwarz, A. Goriachko, H. Over, S. Gsell, M. Schreck, H. Sachdev, T. Greber, and J. Osterwalder, "Boron nitride nanomesh: Functionality from a corrugated monolayer," *Angewandte Chemie International Edition*, vol. 46, no. 27, pp. 5115–5119. [Online]. Available: https://onlinelibrary.wiley.com/doi/abs/10.1002/anie.200700234

[37] M. Will, N. Atodiresei, V. Caciuc, P. Valerius, C. Herbig, and T. Michely, "A monolayer of hexagonal boron nitride on ir(111) as a template for cluster superlattices," *ACS Nano*, vol. 12, no. 7, pp. 6871–6880, Jul. 2018. [Online]. Available: https://doi.org/10.1021/acsnano.8b02127

[38] D. Usachov, A. Fedorov, O. Vilkov, V. K. Adamchuk, L. V. Yashina, L. Bondarenko, A. A. Saranin, A. Grüneis, and D. V. Vyalikh, "Experimental and computational insight into the properties of the lattice-mismatched structures: Monolayers of h-BN and graphene on Ir(111)," , vol. 86, no. 15, p. 155151, Oct. 2012.

[39] M. Petrovic, U. Hagemann, M. H. von Hoegen, and F.-J. M. zu Heringdorf, "Microanalysis of single-layer hexagonal boron nitride islands on ir(111)," *Applied Surface Science*, vol. 420, pp. 504 – 510, 2017. [Online]. Available: http://www.sciencedirect.com/science/article/pii/S0169433217314782

[40] P. Valerius, C. Herbig, M. Will, M. A. Arman, J. Knudsen, V. Caciuc, N. Atodiresei, and T. Michely, "Annealing of ion-irradiated hexagonal boron nitride on ir(111)," *Phys. Rev. B*, vol. 96, p. 235410, Dec 2017. [Online]. Available: https://link.aps.org/doi/10.1103/PhysRevB.96.235410

[41] L. Meng, R. Wu, L. Zhang, L. Li, S. Du, Y. Wang, and H.-J. Gao, "Multi-oriented moiré superstructures of graphene on ir(111): experimental observations and theoretical models," *Journal of Physics: Condensed Matter*, vol. 24, no. 31, p. 314214, 2012. [Online]. Available: http://stacks.iop.org/0953-8984/24/i=31/a=314214

[42] J. Gómez Díaz, Y. Ding, R. Koitz, A. P. Seitsonen, M. Iannuzzi, and J. Hutter, "Hexagonal boron nitride on transition metal surfaces," *Theoretical Chemistry Accounts*, vol. 132, no. 4, p. 1350, Feb 2013. [Online]. Available: https://doi.org/10.1007/s00214-013-1350-z